Title

Aster-dependent nonvesicular transport facilitates dietary cholesterol uptake

Journal

Science, 382(6671)

ISSN

0036-8075

Authors

Ferrari, Alessandra
Whang, Emily
Xiao, Xu
et al.

Publication Date

2023-11-10

DOI

10.1126/science.adf0966

Peer reviewed

HHS Public Access

Author manuscript

Science. Author manuscript; available in PMC 2024 May 06.

Published in final edited form as:

Science. 2023 November 10; 382(6671): eadf0966. doi:10.1126/science.adf0966.

Aster-dependent non-vesicular transport facilitates dietary cholesterol uptake

Alessandra Ferrari[1,2,†], **Emily Whang**[1,2,3,†], **Xu Xiao**[1,2], **John P. Kennelly**[1,2], **Beatriz Romartinez-Alonso**[4], **Julia J. Mack**[5], **Thomas Weston**[5,6], **Kai Chen**[7,8], **Youngjae Kim**[9], **Marcus J. Tol**[1,2], **Lara Bideyan**[1,2], **Alexander Nguyen**[1,2,10], **Yajing Gao**[1,2], **Liujuan Cui**[1,2], **Alexander H. Bedard**[1,2], **Jaspreet Sandhu**[1,11], **Stephen D. Lee**[1,2], **Louise Fairall**[4], **Kevin J. Williams**[2,12], **Wenxin Song**[5,6], **Priscilla Munguia**[5,6], **Robert A. Russell**[13], **Martin G. Martin**[3], **Michael E. Jung**[9], **Haibo Jiang**[7,8], **John W.R. Schwabe**[4], **Stephen G. Young**[5,6], **Peter Tontonoz**[1,2,*]

[1]Department of Pathology and Laboratory Medicine, University of California, Los Angeles; Los Angeles, CA 90095, USA

[2]Department of Biological Chemistry, University of California, Los Angeles; Los Angeles, CA 90095, USA

[3]Pediatric Gastroenterology, Hepatology, and Nutrition, David Geffen School of Medicine, University of California, Los Angeles; Los Angeles, CA 90095, USA

[4]Institute for Structural and Chemical Biology, University of Leicester, Leicester LE1 7RH, UK

[5]Department of Medicine, Division of Cardiology, University of California, Los Angeles; Los Angeles, CA, 90095, USA

[6]Department of Human Genetics, University of California, Los Angeles; Los Angeles, CA 90095, USA

[7]Department of Chemistry, The University of Hong Kong, Hong Kong, 999077, China

[8]School of Molecular Sciences, The University of Western Australia, 35 Stirling Hwy, Crawley WA 6009, Australia

[9]Department of Chemistry, University of California, Los Angeles; Los Angeles, CA 90095, USA

[*]Corresponding author: ptontonoz@mednet.ucla.edu.

[†]These authors contributed equally.

Author contributions:
Conceptualization: AF, EW, PT
Methodology: AF, EW, XX, JPK, SDL, AN, TW, LF, MGM, RAR, LC, AB, KW
Investigation: AF, EW, XX, JPK, BRA, JJM, TW, KC, JS, MJT, LB, AN, YK, YG, PM, WS
Visualization: AF, EW, PT
Funding acquisition: SGY, PT
Project administration: PT
Supervision: MEJ, HJ, JWRS, SGY, PT
Writing – original draft: AF, EW, PT
Writing – review & editing: AF, EW, MEJ, HJ, JWRS, SGY, PT

Competing interests: Authors declare that they have no competing interests.

Data and materials availability: Source data for all figures are provided with the paper. Sequencing data have been deposited to GEO (GSE206780). The crystal structure has been submitted to the PDB database, PDB ID code 8AXW. All unique biological materials used are readily available from the authors or from standard commercial sources.

[10]Vatche and Tamar Manoukian Division of Digestive Diseases, Department of Medicine David Geffen School of Medicine, University of California, Los Angeles; Los Angeles, CA 90095, USA

[11]Molecular Biology Institute, University of California, Los Angeles, Los Angeles, CA 90095, USA

[12]UCLA Lipidomics Core, University of California, Los Angeles, Los Angeles, CA 90095, USA

[13]National Deuteration Facility, Australian Nuclear Science and Technology Organisation, Lucas Heights, Australia

Abstract

Intestinal absorption is an important contributor to systemic cholesterol homeostasis. Niemann-Pick C1 Like 1 (NPC1L1) assists in the initial step of dietary cholesterol uptake, but how cholesterol moves downstream of NPC1L1 is unknown. Here we show that Aster-B and Aster-C are critical for non-vesicular cholesterol movement in enterocytes. Loss of NPC1L1 diminishes accessible plasma membrane (PM) cholesterol and abolishes Aster recruitment to the intestinal brush border. Enterocytes lacking Asters accumulate PM cholesterol and show endoplasmic reticulum (ER) cholesterol depletion. Aster-deficient mice have impaired cholesterol absorption and are protected against diet-induced hypercholesterolemia. Finally, the Aster pathway can be targeted with a small molecule inhibitor to manipulate cholesterol uptake. These findings identify the Aster pathway as a physiologically important and pharmacologically tractable node in dietary lipid absorption.

One-Sentence Summary:

Aster non-vesicular transport is a targetable pathway for regulation of dietary cholesterol absorption.

The intestine regulates systemic lipid homeostasis by gating dietary cholesterol intake (1). Cholesterol is absorbed by enterocytes and packaged into chylomicrons, which are released into the lymphatics and ultimately reach the systemic circulation (2). Most of the cholesterol in chylomicrons is esterified, and cholesterol ester (CE) is necessary for chylomicron packaging. Free cholesterol deposited into the inner leaflet of the apical PM by NPC1L1 must subsequently move to the ER to be esterified by ACAT2 (3–5). Niemann-Pick C1-Like 1 (NPC1L1) is an important mediator of intestinal cholesterol uptake (6, 7), but how cholesterol is delivered to the enterocyte ER for esterification remains to be defined.

NPC1L1 is a target of the drug ezetimibe (EZ) (8–10). The combination of EZ and a statin further reduces cardiovascular events compared to statin alone (10), validating the intestine as a therapeutic target for the regulation of cholesterol homeostasis. EZ was initially discovered as an inhibitor of ACAT2 (11). Its profound effects on cholesterol absorption led to its FDA approval even before the discovery that it inhibits NPC1L1. Genetic ablation of NPC1L1 or EZ administration impairs cholesterol absorption (6). Treatment with EZ protects mice from diet-induced hypercholesterolemia and atherosclerosis (1, 3, 12, 13). Structural analyses have revealed that the N-terminal domain of NPC1L1 possesses a cavity that accommodates cholesterol (14–16). Cholesterol moves through this channel to diffuse into the lipid bilayer. EZ binds within the channel, thereby blocking cholesterol

deposition. Despite the importance of the NPC1L1-ACAT2 axis for cholesterol homeostasis, how cholesterol received by NPC1L1 at the PM ultimately reaches the ER is unresolved (17–24).

Aster proteins (Aster-A, -B, and -C; encoded by *Gramd1a, Gramd1b,* and *Gramd1c*) bind cholesterol and facilitate its movement between membranes (25–27). Members of this family have a central cholesterol-binding pocket that is flanked by a GRAM domain at the N-terminus and an ER transmembrane domain at the C-terminus. The GRAM domain binds the PM in response to cholesterol loading, allowing Asters to transfer cholesterol down a concentration gradient from the PM to the ER. The role of non-vesicular cholesterol transport in cell function is highly cell-type specific. In mice, Aster-B is required for CE storage and corticosteroid synthesis in the adrenal cortex (25), while Aster-C is important for hepatic reverse cholesterol transport (28).

Here we show NPC1L1 and Asters and play sequential, non-redundant roles in the delivery of dietary cholesterol from the intestinal lumen to the enterocyte ER. Asters are recruited to the enterocyte PM upon cholesterol loading, and loss of their expression impairs CE production. Treatment of mice with a small-molecule Aster inhibitor reduces the systemic absorption of dietary cholesterol, and mice lacking Asters in the intestine are protected from diet-induced hypercholesterolemia. Our findings support a model in which the principal function of NPC1L1 is to enrich the enterocyte PM with dietary cholesterol. This enrichment facilitates the recruitment of Asters to the PM where they mediate non-vesicular cholesterol trafficking to the ER. These findings identify intestinal Asters as key players in dietary lipid absorption and potential targets for the control of cholesterol homeostasis.

Results

Intestinal Aster expression is regulated by Liver X Receptors

Transcripts for Aster-A, -B, and -C are expressed in the small intestine (SI) (Fig. 1A), and RNA-seq from proximal jejunal scrapings of C57BL6/J mice confirmed robust expression of *Gramd1b* and *Gramd1c* and low expression of *Gramd1a* (Fig. S1A). The most abundant *Gramd1c* transcript in the SI encodes a truncated Aster-C lacking the N-terminal GRAM domain. RNA-seq also revealed the presence of two transcripts for *Gramd1b* in the intestine; one was the same as that identified previously in macrophages (25), while the other had an extended N-terminal region upstream of the GRAM domain (Fig. S1A). An intestine-specific promoter in the *Gramd1b* locus (chr9: 40465470–40465756) defined the longer variant. Absolute quantification of *Gramd1* transcripts in intestinal epithelial cells confirmed those for Aster-B and -C were most abundant (Fig. S1B). Aster-B was expressed along the entire length of the SI (duodenum to the ileum) (Fig. S1C). In Caco-2 cells, transcripts for Aster-B and -C were induced upon differentiation (Fig. S1D). Liver X receptor transcription factors are key regulators of cholesterol metabolism (29, 30). Treatment of WT mice with the LXR agonist GW3965 induced the expression of all three Asters in the SI (Fig. S1E), consistent with a role for the Aster pathway in intestinal cholesterol flux.

Aster proteins facilitate cholesterol uptake in the small intestine

To visualize endogenous Aster-B movement in enterocytes, we used CRISPR-Cas9 editing to insert a 3×HA tag into the mouse *Gramd1b* locus (Fig. S1F and G). Immunohistochemistry of intestinal tissue revealed that HA-Aster-B was enriched in the villi of the jejunum with lower expression in the crypts (Fig. S1H). To study Aster localization in culture we derived enteroids from intestinal crypts of HA-Aster-B mice. Confocal imaging demonstrated that Aster-B was recruited to the PM in response to loading with methyl-β-cyclodextrin (MβCD)–cholesterol (Fig. 1B). Accordingly, immunohistochemistry showed a greater distribution of HA-Aster-B at the brush border of enterocytes 1 h after intra-gastric gavage with cholesterol in corn oil versus corn oil alone (Fig. 1DC

To explore the function of Asters in intestinal physiology, we generated global knockout mice for Aster-B (B-KO), Aster-C (C-KO), or both (B/C-KO) (Fig. S2A and B). Deletion of Asters was verified in jejunal scrapings (Fig. S2C, D, and E). The SI from B/C-KO mice had no obvious histological abnormalities (Fig. S2F), and body weight and intestinal length showed minimal differences across genotypes (Fig. S2G). To evaluate the role of Asters in cholesterol uptake, we administered [^{14}C]cholesterol by gastric gavage and measured radioactivity in SI 2 hours later. No differences in [^{14}C]cholesterol absorption were detected in single-KO mice (Fig. S2 H–M), but we observed markedly reduced absorption in the proximal intestine of B/C-KO mice (Fig. 1D, Fig. S2N and O). B/C-KO mice also had reduced amounts of [^{14}C]cholesterol in the plasma and liver 2 h after gavage (Fig. 1, E and F).

To confirm that this impairment in cholesterol absorption resulted from Aster deficiency in enterocytes, we generated mice with tamoxifen-inducible, intestine-specific deletion of Aster-B (I-B-KO), Aster-C (I-C-KO), or both (I-B/C-KO) by intercrossing double “floxed” mice with Villin-Cre^{ERT2} transgenic mice (Fig. S3A–F). I-B/C KO mice displayed normal crypt cell proliferation as revealed by OLFM4 staining (Fig. S3G). Minimal differences in body weight or SI length were observed between control and I-B/C KO mice (Fig. S3H). Thus, loss of Aster expression does not appear to compromise intestinal development.

Cholesterol uptake was similar in I-B KO, I-C-KO, and littermate control mice (Fig. S3I–N). However, I-B/C-KO mice had reduced [^{14}C]cholesterol absorption compared to floxed controls (similar to global B/C-KO mice) (Fig. 1G–I). Cumulative counts in the proximal tract (Fig. 1G) were reduced, while counts in medial and distal regions were not different (Fig. S3O, P). Fractional cholesterol absorption, assessed by fecal dual isotope labeling, confirmed impaired cholesterol absorption in I-B/C-KO mice (Fig. 1J). By contrast, there were no detectable reductions in ^{14}C counts in intestinal segments, plasma, and liver of I-B/C-KO mice after an oral gavage of [^{14}C]triolein (Fig. S4A–D). Glucose absorption was not impacted in I-B/C-KO mice (Fig. S4E). Thus, loss of Aster function in enterocytes selectively impairs cholesterol absorption.

Next, we followed the appearance of orally administered [^{14}C]cholesterol in the plasma over 12 h. There was a marked reduction in ^{14}C counts in the plasma of B/C-KO mice, while B-KO and C-KO mice exhibited an intermediate phenotype (Fig. 1K). We also injected mice with the lipoprotein lipase inhibitor Poloxamer-407, gavaged them with [^{14}C]cholesterol,

and collected plasma up to 4 h post gavage. The appearance of [^{14}C]cholesterol in the plasma over time, as well as total plasma cholesterol levels, was reduced in I-B/C-KO mice (Fig. 1L and 1M).

Non-vesicular cholesterol transport enables intestinal CE production

Adequate CE is required for chylomicron production by the intestine. We hypothesized that Aster-mediated non-vesicular transport from the PM to the ER facilitates cholesterol esterification and subsequent incorporation into chylomicrons. We used nanoscale secondary ion mass spectrometry (NanoSIMS) imaging to visualize cholesterol uptake and intracellular distribution by enterocytes (31, 32). Mice received an intra-gastric gavage of [^{13}C]fatty acids and [^{2}H]cholesterol in olive oil. Biopsies from the duodenum were harvested 2 h later. Backscattered electron images of duodenal sections verified the integrity of intestinal villi (Fig. 2A and Fig. S5A). NanoSIMS images of the same sections (Fig. 2A, Fig. S5A) revealed reduced amounts of ^{2}H in medial and distal segments of the duodenum in B/C-KO mice. Quantification of $^{13}C^{-}$ and $^{2}H^{-}$ secondary ions confirmed reduced cholesterol uptake by enterocytes lacking Asters (Fig. 2B, Fig. S5B).

Previous studies showed that in macrophages (33) and hepatocytes (28) Asters specifically recognize the accessible pool of PM cholesterol (34, 35). To prove that Asters transfer accessible cholesterol from PM to ER in intestinal epithelial cells, we stained WT and Aster-B/C KO enteroids with ALOD4, a bacterial peptide that selectively binds to accessible cholesterol. Confocal microscopy revealed enhanced ALOD4 staining at the PM of Aster-B/C KO enteroids loaded with MβCD-cholesterol (Fig. 2C), consistent with reduced cholesterol movement to ER. Accordingly, lipidomic analysis of jejunal scrapings revealed reduced CE in B/C-KO mice after feeding (Fig. 3A). Other lipid species were not affected by Aster deficiency (Fig. S6A). Consistent with these findings, ^{14}C-labeled CE accumulation was reduced in the proximal jejunum of Aster-deficient mice 2 h after oral administration of [^{14}C]cholesterol in olive oil (Fig. 3B). The level of free [^{14}C]cholesterol was similar between groups (Fig. S6B). SREBP-2 target gene expression was higher in global B/C-KO than in WT mice, both in fasted and refed states (Fig. 3C, D), consistent with reduced ER cholesterol. Similar findings were observed in jejunal scrapings of I-B/C-KO mice (Fig. 3E). Protein levels of SREBP-2 targets in duodenal scrapings were correspondingly elevated in B/C-KO mice (Fig. 3F). We also observed upregulation of *Srebf2* and its targets in jejunal scrapings in B/C-KO mice fed a high-cholesterol (HC) diet (1.25% cholesterol) (Fig. S6C). Thus, even in the setting of increased dietary cholesterol, cholesterol synthesis was activated in B/C-KO mice. We did not observe changes in SREBP-2 pathway expression in the jejunum of global (Fig. S6, D and E) or intestinal-specific (Fig. S6, F and G) single-KO mice.

Plasma levels of ApoB48 after refeeding with a HC diet were not different between groups (Fig. 3G and H), despite lower plasma cholesterol levels in I-B/C KO mice (Fig. 3I). Plasma triglyceride levels were also comparable (Fig. S6H), consistent with our observation that fatty acid absorption was unaffected by loss of Asters (Fig. S4A–D). These findings suggest that Aster deficiency reduces cholesterol content in chylomicrons, but does not alter the process of chylomicron assembly and release per se. In support of this conclusion, there

were fewer ^{14}C counts in the chylomicron fraction of plasma isolated 2 h after oral gavage of [^{14}C]cholesterol in I-B/C KO mice versus control mice (Fig. 3J). To show that this decrease in cholesterol was due to a reduction in CE, we analyzed chylomicron composition in mice gavaged with d4-cholesterol and injected with Poloxamer-407. I-B/C KO mice had reduced d4-CE in chylomicrons (Fig. 3K) without changes in d4-cholesterol compared to floxed control mice (Fig. 3L). Unlabeled CE species were also lower, while unlabeled cholesterol was not different (Fig. S6I, J).

Loss of Asters protects against diet-induced hypercholesterolemia

Next, we investigated whether intestinal Aster deficiency affected systemic cholesterol homeostasis. After 21 days of a HC diet, we observed a modest decrease in the weight of global B/C-KO mice (Fig. 4A), accompanied by reduced fasting plasma cholesterol levels (Fig. 4B). Liver cholesterol levels were also reduced (Fig. 4C). We also found lower fasting plasma cholesterol levels in intestine-specific Aster-KO mice but no change in body weight (Fig. 4D, E). FPLC fractionation of plasma revealed lower cholesterol levels in the VLDL/LDL and HDL fractions from Aster-KO mice (Fig. 4F). Plasma triglyceride levels were similar between groups (Fig. S7A and B). SREBP-2 pathway gene and protein expression (Fig. 4G–I) was elevated in global B/C-KO and I-B/C-KO mice compared to controls. Thus, de novo cholesterol synthesis was activated in KO intestine even in the setting of excess dietary cholesterol (Fig. 4H, 4I). Lipidomic analyses revealed reduced CE in I-B/C-KO enterocytes on the HC diet (Fig. 4J), without changes in other lipid species (Fig. S7C). We did not observe changes in body weight (Fig. S7D) or lipid levels in Aster single-KO mice after 21 days of HC diet (Fig. S7 E and F), nor did we observe a change in SREBP-2 targets (Fig. S7G).

Ezetimibe binds to Aster-B and Aster-C

Because both Aster deficiency and EZ reduce cholesterol absorption, we tested whether Asters might bind EZ. Using competition assays for 22-NBD-cholesterol binding, we found that EZ bound to Aster-B and Aster-C (Fig. 5A) with moderate affinity, but exhibited minimal binding to Aster-A and StARD1 (Fig. S8A). Next, we solved the crystal structure, at 1.6 Å resolution, of the ASTER domain from Aster-C complexed to EZ. The overall structure of the Aster-C domain revealed a canonical curved seven-stranded beta-sheet that forms a cavity to accommodate EZ (Fig. 5B, Table S3). The cavity is closed by a long carboxyl-terminal helix and two shorter helices. The electron density map and the simulated annealing composite omit map highlighted additional volume within the binding cavity that accommodates a glycerol molecule, and density for part of a PEG4000 molecule from the cryo-protectant and crystallization buffer (Fig. S8B, S8C, respectively). The electron density for the PEG is stronger at the end in proximity to the EZ ligand and becomes weaker at the other end, presumably due to disorder. Thus, the precise translational position of the PEG is uncertain. Modeling of ezetimibe-glucuronide, the active metabolite of EZ, in the pocket suggested potential capacity for binding, since the glucuronide group is oriented toward an opening of the pocket (Fig. S8D). Circular dichroism (CD) spectra of the Aster-A, -B, and -C domains revealed that Aster-B and -C were thermally stabilized by EZ binding, whereas Aster-A was not (Fig. S8E). Cholesterol and U18666A were included as positive controls (25, 36).

To investigate the molecular basis for selective binding of EZ to Aster-C, we compared the structures of Aster-C:EZ and Aster-A:25.-hydroxycholesterol (Fig. 5C). Many of the residues involved in ligand interactions are conserved in Aster-A and Aster-C (Fig. S8F). However, leucine 400 and phenylalanine 405 in the ASTER domain of Aster-A appeared to represent a steric hindrance to EZ binding (Fig. 5D), while alanine 357 and isoleucine 362 in the ASTER domain of Aster-C left ample space for EZ binding (Fig. 5D). The importance of the specific amino acids on EZ binding was interrogated by mutagenesis and evaluation of thermal stability by CD. The two residues that appeared to hinder EZ binding in Aster-A were changed to the residues found in Aster-C (L400A_F405I). Conversely, the residues that appeared to be important for accommodating EZ binding in Aster-C were changed to those in Aster-A (A357L_I362F) which potentially prevent binding. The Aster-A mutant L400A_F405I, as well as the single mutant L400A, reduced Aster-A thermal stability (Fig. S8G), but the stability was increased by EZ. The thermal stability upon EZ binding was unchanged in the F405I mutant (Fig. S8G), suggesting that L400A is crucial for binding selectivity. These results were corroborated by the Aster-C mutants, where A357L_I362F and A357L alone increased thermal stability of the protein, while I362F had no effect. The thermal stability of the A357L Aster-C mutant did not change with EZ binding, implying a weak interaction between EZ and that mutant (Fig. S8G).

Asters cooperate with NPC1L1 in intestinal cholesterol absorption

The ability of Aster-B and -C to bind EZ suggested that they may act in concert with NPC1L1 to promote cholesterol absorption. To test this hypothesis, we fed mice a moderate-cholesterol control diet or a moderate-cholesterol diet containing 0.01% EZ for 3 days (Fig. S9A). As expected, EZ decreased CE content and fractional cholesterol absorption by the fecal dual isotope method in WT mice (Fig. 6A–C). Aster-B/C-KO and I-B/C-KO mice showed decreased CE content (Fig. 6A, B) and fractional cholesterol absorption (Fig. 6C); EZ treatment led to a further reduction. Aster deficiency did not provide an additional decrease in CE or cholesterol absorption in EZ-treated mice (Fig. 6A–C). However, gene-expression and protein analyses revealed stronger activation of the SREBP-2 pathway in Aster-B/C-KO mice on the EZ diet compared to either Aster-B/C KO mice or EZ-treated WT mice (Fig. S9B and Fig. 6D).

Cholesterol loading triggers Aster-B movement to the PM (Fig. 1B). EZ blocks the channel within NPC1L1 required for cholesterol deposition into the PM (15). Therefore, we theorized that EZ would attenuate Aster translocation to the PM by preventing the expansion of the accessible cholesterol pool. To test this idea, 3×HA-Aster-B mice were fed control or EZ diet for 3 days and gavaged with vehicle or EZ 30 minutes prior to a second gavage of cholesterol in corn oil. Small intestines were harvested 1 h later. Remarkably, EZ completely prevented the recruitment of Aster-B to the brush border after cholesterol gavage (Fig. 6E). Next, we everted enteroids such that the apical PM was facing out (37) and administered mixed micelles (MM) containing cholesterol in the presence of vehicle or EZ. Immunofluorescence microscopy confirmed that recruitment of HA-Aster-B to the apical PM of enteroids was induced by cholesterol loading in MM but reduced by EZ (Fig. S9C). Furthermore, we found decreased ALOD4 staining in enteroids derived from NPC1L1-KO mice loaded with MM cholesterol, indicating that NPC1L1 is required to saturate the PM

with accessible cholesterol (Fig. 6F, upper panels). When enteroids were loaded with MβCD cholesterol, ALOD4 binding was not different between NPC1L1KO and WT enteroids (Fig. 6F, bottom panels). Thus, delivery of cholesterol in MβCD effectively bypasses the function of NPC1L1.

We then crossed 3×HA-Aster-B mice to NPC1L1 WT (HA-B-NPC1L1 WT) or NPC1L1 KO (HA-B-NPC1L1 KO) animals. In enteroids derived from these mice, NPC1L1 deletion reduced 3×HA-Aster-B recruitment to the PM after MM cholesterol loading, but had no effect on MβCD cholesterol loading (Fig. S9D). Analysis of HA-B-NPC1L1 WT and HA-B-NPC1L1 KO mice confirmed that genetic ablation of NPC1L1 abolished Aster-B movement to the brush border in response to cholesterol loading, mirroring the effects of EZ (Fig. 6G and S9E). These results substantiate the hypothesis that EZ prevents Aster translocation to the brush border via NPC1L1 blockade. They further show that EZ prevents the saturation of cholesterol at the apical membrane by inhibiting NPC1L1 rather than Aster-B inhibition.

Next, we generated a McA-RH7777 CRL-1601 cell line stably expressing NPC1L1-EGFP and HA-Aster-B fusion proteins. Following cholesterol depletion, NPC1L1 partially localized to PM, while Aster-B was confined to the ER (Fig. S9F). MβCD-cholesterol loading caused internalization of NPC1L1-EGF and, concomitantly, the movement of HA-Aster-B to ER-PM contact sites. This contrasting behavior of NPC1L1 and Aster in response to cholesterol loading argues against a direct physical interaction between the two proteins during cholesterol import.

Pharmacological Aster inhibition reduces intestinal cholesterol uptake

Previous work from our laboratory identified a small molecule, AI-3d, that potently inhibits Aster-A, -B, and -C (36). We tested the ability of AI-3d to mimic the effects of Aster deficiency on cholesterol absorption. First, we pretreated enteroids with AI-3d and assessed accessible cholesterol with the ALOD4 probe. Treatment of WT enteroids with AI-3d and MβCD cholesterol led to an accumulation of accessible cholesterol, while AI-3d had no additional effect on ALOD4 binding in B/C-KO enteroids (Fig. 7A, fig. S10A). AI-3d generated a similar effect in human jejunal enteroids (Fig. 7B), indicating that AI-3d inhibits both human and murine Asters. We also compared the effects of AI-3d on WT and NPC1L1 KO enteroids. When enteroids were loaded with MM cholesterol, AI-3d treatment increased ALOD4 binding only in NPC1L1 WT cells (Fig. S10B). However, when enteroids were loaded with MβCD-cholesterol, AI-3d treatment increased ALOD4 binding similarly in WT and NPC1L1 KO cells (Fig. S10C). Thus, NPC1L1 deposits micellular cholesterol into the PM to expand the accessible pool and MβCD bypasses this function.

Finally, we assessed the impact of AI-3d on cholesterol transport to the ER. Consistent with our results in Aster-KO mice, AI-3d increased SREBP-2 target gene expression in human enteroids (Fig. 7C) and differentiated Caco-2 cells (Fig. S10D). We further tested the effect of AI-3d on cholesterol absorption in vivo. C57BL/6J mice were pretreated with AI-3d or EZ for 1 h, gavaged with [^{14}C]cholesterol, and given an intraperitoneal injection of Poloxamer-407. EZ treatment and pharmacologic inhibition of Asters both reduced dietary cholesterol absorption into the circulation (Fig. 7D).

Next, we evaluated the impact of Aster inhibition on mice fed a moderate-cholesterol diet (Fig. S10E). AI-3d did not affect body weight or intestinal length (Fig. S10 F–H), supporting the absence of toxicity. Lipidomic analysis revealed reduced CE in jejunal scrapings from NPC1L1 KO compared to WT mice. Aster inhibition by AI-3d lowered levels of jejunal CE similarly in WT and NPC1L1 KO, indicating that AI-3d does not act through NPC1L1 (Fig. 7E). Gene expression analysis showed a further induction of SREBP2 targets in NPC1L-KO mice treated with AI-3d (Fig. 7F).

Finally, we tested the effect of AI-3d on NPC1L1 recycling using McA-RH7777 CRL-1601 cells stably expressing an NPC1L1-EGFP fusion protein. Consistent with published data (17), we observed that NPC1L1-EGFP was present within a recycling compartment when both vehicle-treated and AI-3d treated cells were cultured in full serum (Fig. S10I, left panels). In response to cholesterol depletion by MβCD, the signal in both cell types moved to the PM (Fig. S10I, middle panels). Conversely, MβCD-cholesterol loading led to the relocation of NPC1L1-EGFP to endosomes (Fig. S10I, right panels). These results indicate that AI-3d treatment does not interfere with the process of NPC1L1 recycling, further supporting the conclusion that AI-3d inhibits cholesterol absorption by targeting Asters.

Discussion

The involvement of NPC1L1 in facilitating the entry of cholesterol into enterocytes and the role of ACAT2 in cholesterol esterification are well documented, and both proteins are recognized to be key players in the process of cholesterol absorption (5, 6). However, how cholesterol that enters the cell via NPC1L1 reaches the ER for esterification and regulation of cholesterol synthesis has been a long-standing mystery. Here we solve that mystery by showing that Aster-B and -C link NPC1L1 to ACAT2 by facilitating non-vesicular cholesterol transport to the ER following uptake by NPC1L1 at the enterocyte PM. Combined deletion of Aster-B and -C impairs the movement of dietary cholesterol to ER in enterocytes, as evidenced by expansion of the accessible PM cholesterol pool, reduced CE formation, and activation of the SREBP-2 pathway for cholesterol synthesis. Physiologically, inhibition of Aster non-vesicular transport reduces cellular cholesterol stores and impairs the incorporation of CE into chylomicrons.

Our results suggest that cholesterol homeostasis in enterocytes requires both NPC1L1-mediated cholesterol deposition into the PM and subsequent Aster-mediated transport to the ER. Since NPC1L1 is the gatekeeper that controls the first step of cholesterol uptake, cholesterol absorption is reduced when NPC1L1 is blocked by EZ. In this context, Aster deletion does not further decrease absorption, because the apical PM cholesterol available for transfer is limited. At the same time, the observation that CE production in the ER is markedly impaired by Aster deletion even when NPC1L1 is present argues against a dominant role for NPC1L1 itself in cholesterol transport to the ER. Thus, NPC1L1 and Asters function in series to move cholesterol from the diet into the circulation. EZ binds to Aster-B and -C with moderate affinity, raising the possibility that inhibition of Aster function could contribute to EZ's capacity to inhibit cholesterol absorption. However, EZ binding to Aster was not sufficient to block non-vesicular cholesterol transport in vivo in our studies, as Aster deletion further reduced ER cholesterol delivery in the presence of EZ.

The recruitment of Asters to the PM depends on the cholesterol and phosphatidylserine content in the inner leaflet (25, 26, 33). Our results support the notion that Aster-mediated non-vesicular transport relies on NPC1L1 to deposit cholesterol into the apical enterocyte PM, rather than on a direct physical interaction with NPC1L1. In support of this concept, micelle-derived cholesterol cannot contribute to the expansion of the accessible pool, and Aster proteins do not translocate to the enterocyte PM when NPC1L1 is deleted or inhibited by EZ. However, when NPC1L1 is bypassed by delivering cholesterol directly to the PM with MβCD, Aster is recruited normally.

Previous studies demonstrated that NPC1L1 is internalized when enterocytes are exposed to dietary cholesterol (38). This observation has led to the suggestion that vesicular transport by NPC1L1-containing vesicles is important for cholesterol delivery to the ER (21, 24, 38). However, formal tests of the relative contribution of vesicular and non-vesicular cholesterol transport mechanisms downstream of NPC1L1 have been lacking. Our data indicate that the primary function of NPC1L1 is to deposit dietary cholesterol into the enterocyte PM. NPC1L1 is a homolog of the Niemann-Pick C1 (NPC1) protein that mediates cholesterol export from lysosomes following endocytosis of LDL cholesterol (39). Molecular studies have established that NPC1 acts to enrich cholesterol in the lysosomal membrane (40, 41), and that such enrichment allows for the subsequent transfer of cholesterol to PM by cytoplasmic non-vesicular transfer proteins (42). Our results suggest that the structurally related NPC1 and NPC1L1 perform analogous functions: both enrich membrane cholesterol to facilitate the recruitment of non-vesicular transporters. We propose that the sterol-regulated endocytosis of NPC1L1 could represent a feedback mechanism to limit cholesterol absorption, rather than a major mechanism for vesicular cholesterol transfer to the ER. However, our data do exclude the participation of other vesicular and non-vesicular pathways in the intracellular movement of cholesterol in enterocytes. Nor do they exclude the possibility that Aster proteins retrieve cholesterol, directly or indirectly, from NPC1L1-rich endosomes.

Intestinal non-vesicular cholesterol transport could be a target for treating diet-induced hypercholesterolemia. First, Aster-B/C knockout mice have low plasma cholesterol levels when fed a western diet enriched in cholesterol. Second, we showed that the Aster pathway can be targeted pharmacologically to reduce cholesterol absorption. The inhibitor AI-3d, which had been shown previously (36) to inhibit Aster-mediated non-vesicular transport in vitro, reduced cholesterol transport to the ER and expanded the pool of accessible cholesterol at PM of intestinal enteroids. Finally, treatment of mice with AI-3d inhibited cholesterol absorption. These findings identify the Aster pathway as a potentially attractive pathway for limiting intestinal cholesterol absorption and reducing plasma cholesterol.

Materials and methods summary

Detailed materials and methods can be found in the supplementary materials, including generation of murine models, experimental conditions for in vivo studies, histology and immunohistochemistry, cholesterol absorption assays, lipid measurements, chylomicron isolation, isolation of intestinal epithelial cells, protein isolation and immunoblot assays, RNA extraction and gene expression analysis, in vivo back scattered electron (BSE)

microscopy and NanoSIMS, isolation of murine crypts, culture and expansion of enteroids (basolateral-out or apical-out), culture of human intestinal epithelial cells on transwell membranes for gene expression, immunofluorescence microscopy, purification and fluorophore conjugation of ALOD4, immortalized cell cultures (Caco-2 and McArdle RH7777), protein expression and purification, crystallization and X-ray structure determination, and circular dichroism.

Supplementary Material

Refer to Web version on PubMed Central for supplementary material.

Acknowledgments:

We thank Loren Fong, Paul Kim and Elmira Tokhtaeva for the technical assistance. We also thank all members of the Tontonoz, Tarling-Vallim, Edwards, Villanueva, Young and Bensinger labs at UCLA for useful advice and discussions and for sharing reagents and resources. We thank G. Su and the UCLA Lipidomics and Y. Li and the UCLA Translational Pathology Core Laboratory. pALOD4 was a gift from Arun Radhakrishnan (Addgene plasmids # 111026). We thank Bao-Liang Song at Wuhan University for the NPC1L1-EGFP construct and NPC1L1 KO mice. We thank Tamim Darwish for supporting the production of [2H]cholesterol.

Funding:

This work was supported by:

National Institutes of Health grant R01 DK126779 to PT

National Institutes of Health grant P01 HL146358 to SGY

Transatlantic Network of Excellence, Leducq Foundation, 19CDV04

American Diabetes Association Postdoctoral fellowship 1-19-PDF-043-RA to AF

Ermenegildo Zegna Founder's Scholarship 2017 to AF

CDI Junior Faculty Career Development Award (CD-JFCD-07012019) to EW

CDI NIH K12 Junior Faculty Career Development Grant (CDI-K12-07012023) to EW

Today's and Tomorrow's Children Fund Bridge Grant (CDI-TTCF-07012022) to EW

UCSD-UCLA Diabetes Research Center (DK063491) to EW and PT

American Heart Association Postdoctoral Fellowship 18POST34030388 to XX

American Heart Association Postdoctoral Fellowship 903306 to JPK

Damon Runyon Cancer Research Fellowship (DRG-2424-21) to YG

National Institutes of Health grant T32 DK007180 to AN

The National Collaborative Research Infrastructure Strategy (NCRIS), an Australian Government initiative, to the National Deuteration Facility in Australia.

References and Notes

1. Xie P et al. , Genetic demonstration of intestinal NPC1L1 as a major determinant of hepatic cholesterol and blood atherogenic lipoprotein levels. Atherosclerosis 237, 609–617 (2014). [PubMed: 25463095]

2. Mansbach CM, Siddiqi SA, The Biogenesis of Chylomicrons. Annual Review of Physiology 72, 315–333 (2010).

3. Buhman KK et al. , Resistance to diet-induced hypercholesterolemia and gallstone formation in ACAT2-deficient mice. Nature Medicine 6, 1341–1347 (2000).

4. Nguyen TM, Sawyer JK, Kelley KL, Davis MA, Rudel LL, Cholesterol esterification by ACAT2 is essential for efficient intestinal cholesterol absorption: evidence from thoracic lymph duct cannulation [S]. Journal of Lipid Research 53, 95–104 (2012). [PubMed: 22045928]

5. Zhang J et al. , Tissue-specific knockouts of ACAT2 reveal that intestinal depletion is sufficient to prevent diet-induced cholesterol accumulation in the liver and blood[S]. Journal of Lipid Research 53, 1144–1152 (2012). [PubMed: 22460046]

6. Altmann Scott W et al. , Niemann-Pick C1 Like 1 Protein Is Critical for Intestinal Cholesterol Absorption. Science 303, 1201–1204 (2004). [PubMed: 14976318]

7. Davis HR Jr. et al. , Niemann-Pick C1 Like 1 (NPC1L1) Is the Intestinal Phytosterol and Cholesterol Transporter and a Key Modulator of Whole-body Cholesterol Homeostasis. Journal of Biological Chemistry 279, 33586–33592 (2004). [PubMed: 15173162]

8. Garcia-Calvo M et al. , The target of ezetimibe is Niemann-Pick C1-Like 1 (NPC1L1). Proceedings of the National Academy of Sciences 102, 8132–8137 (2005).

9. Davis HR, Pula KK, Alton KB, Burrier RE, Watkins RW, The synergistic hypocholesterolemic activity of the potent cholesterol absorption inhibitor, ezetimibe, in combination with 3-hydroxy-3-methylglutaryl coenzyme a reductase inhibitors in dogs. Metabolism 50, 1234–1241 (2001). [PubMed: 11586500]

10. Cannon CP et al. , Ezetimibe Added to Statin Therapy after Acute Coronary Syndromes. New England Journal of Medicine 372, 2387–2397 (2015). [PubMed: 26039521]

11. Clader JW, The Discovery of Ezetimibe: A View from Outside the Receptor. Journal of Medicinal Chemistry 47, 1–9 (2004). [PubMed: 14695813]

12. Davis HR, Compton DS, Hoos L, Tetzloff G, Ezetimibe, a Potent Cholesterol Absorption Inhibitor, Inhibits the Development of Atherosclerosis in ApoE Knockout Mice. Arteriosclerosis, Thrombosis, and Vascular Biology 21, 2032–2038 (2001). [PubMed: 11742881]

13. Lee RG et al. , Plasma Cholesteryl Esters Provided by Lecithin:Cholesterol Acyltransferase and Acyl-Coenzyme A:Cholesterol Acyltransferase 2 Have Opposite Atherosclerotic Potential. Circulation Research 95, 998–1004 (2004). [PubMed: 15486318]

14. Hu M et al. , Structural insights into the mechanism of human NPC1L1-mediated cholesterol uptake. Science Advances 7, eabg3188 (2021). [PubMed: 34272236]

15. Huang C-S et al. , Cryo-EM structures of NPC1L1 reveal mechanisms of cholesterol transport and ezetimibe inhibition. Science Advances 6, eabb1989 (2020). [PubMed: 32596471]

16. Long T, Liu Y, Qin Y, DeBose-Boyd Russell A, Li X, Structures of dimeric human NPC1L1 provide insight into mechanisms for cholesterol absorption. Science Advances 7, eabh3997 (2021). [PubMed: 34407950]

17. Ge L et al. , The Cholesterol Absorption Inhibitor Ezetimibe Acts by Blocking the Sterol-Induced Internalization of NPC1L1. Cell Metabolism 7, 508–519 (2008). [PubMed: 18522832]

18. Weinglass Adam B et al. , Extracellular loop C of NPC1L1 is important for binding to ezetimibe. Proceedings of the National Academy of Sciences 105, 11140–11145 (2008).

19. Ge L et al. , Flotillins play an essential role in Niemann-Pick C1-like 1-mediated cholesterol uptake. Proceedings of the National Academy of Sciences 108, 551–556 (2011).

20. Wang L-J et al. , Molecular Characterization of the NPC1L1 Variants Identified from Cholesterol Low Absorbers. Journal of Biological Chemistry 286, 7397–7408 (2011). [PubMed: 21189420]

21. Li P-S et al. , The clathrin adaptor Numb regulates intestinal cholesterol absorption through dynamic interaction with NPC1L1. Nature Medicine 20, 80–86 (2014).

22. Chu B-B et al. , Requirement of Myosin Vb·Rab11a·Rab11-FIP2 Complex in Cholesterol-regulated Translocation of NPC1L1 to the Cell Surface*. Journal of Biological Chemistry 284, 22481–22490 (2009). [PubMed: 19542231]

23. Johnson TA, Pfeffer SR, Ezetimibe-sensitive cholesterol uptake by NPC1L1 protein does not require endocytosis. Molecular Biology of the Cell 27, 1845–1852 (2016). [PubMed: 27075173]

24. Zhang Y-Y et al. , A LIMA1 variant promotes low plasma LDL cholesterol and decreases intestinal cholesterol absorption. Science 360, 1087–1092 (2018). [PubMed: 29880681]
25. Sandhu J et al. , Aster Proteins Facilitate Nonvesicular Plasma Membrane to ER Cholesterol Transport in Mammalian Cells. Cell 175, 514–529 (2018). [PubMed: 30220461]
26. Naito T et al. , Movement of accessible plasma membrane cholesterol by the GRAMD1 lipid transfer protein complex. eLife 8, e51401 (2019). [PubMed: 31724953]
27. Besprozvannaya M et al. , GRAM domain proteins specialize functionally distinct ER-PM contact sites in human cells. eLife 7, e31019 (2018). [PubMed: 29469807]
28. Xiao X et al. , Hepatic nonvesicular cholesterol transport is critical for systemic lipid homeostasis. Nature Metabolism 5, 165–181 (2023).
29. Wang B, Tontonoz P, Liver X receptors in lipid signalling and membrane homeostasis. Nature Reviews Endocrinology 14, 452–463 (2018).
30. Yu L et al. , Expression of ABCG5 and ABCG8 Is Required for Regulation of Biliary Cholesterol Secretion. Journal of Biological Chemistry 280, 8742–8747 (2005). [PubMed: 15611112]
31. Jiang H et al. , High-resolution imaging of dietary lipids in cells and tissues by NanoSIMS analysis[S]. Journal of Lipid Research 55, 2156–2166 (2014). [PubMed: 25143463]
32. He C et al. , NanoSIMS Analysis of Intravascular Lipolysis and Lipid Movement across Capillaries and into Cardiomyocytes. Cell Metabolism 27, 1055–1066.e1053 (2018). [PubMed: 29719224]
33. Ferrari A et al. , Aster Proteins Regulate the Accessible Cholesterol Pool in the Plasma Membrane. Molecular and Cellular Biology 40, e00255–00220 (2020). [PubMed: 32719109]
34. Das A, Brown MS, Anderson DD, Goldstein JL, Radhakrishnan A, Three pools of plasma membrane cholesterol and their relation to cholesterol homeostasis. LID - 10.7554/eLife.02882 [doi] LID - e02882. (2014).
35. Gay A, Rye D, Radhakrishnan A, Switch-like Responses of Two Cholesterol Sensors Do Not Require Protein Oligomerization in Membranes. Biophysical Journal 108, 1459–1469 (2015). [PubMed: 25809258]
36. Xiao X et al. , Selective Aster inhibitors distinguish vesicular and nonvesicular sterol transport mechanisms. Proceedings of the National Academy of Sciences 118, e2024149118 (2021).
37. Co JY et al. , Controlling Epithelial Polarity: A Human Enteroid Model for Host-Pathogen Interactions. Cell Reports 26, 2509–2520.e2504 (2019). [PubMed: 30811997]
38. Xie C et al. , Ezetimibe blocks the internalization of NPC1L1 and cholesterol in mouse small intestine. Journal of Lipid Research 53, 2092–2101 (2012). [PubMed: 22811412]
39. Carstea ED et al. , Niemann-Pick C1 Disease Gene: Homology to Mediators of Cholesterol Homeostasis. Science 277, 228–231 (1997). [PubMed: 9211849]
40. Kwon HJ et al. , Structure of N-Terminal Domain of NPC1 Reveals Distinct Subdomains for Binding and Transfer of Cholesterol. Cell 137, 1213–1224 (2009). [PubMed: 19563754]
41. Qian H et al. , Structural Basis of Low-pH-Dependent Lysosomal Cholesterol Egress by NPC1 and NPC2. Cell 182, 98–111.e118 (2020). [PubMed: 32544384]
42. Wang H et al. , ORP2 Delivers Cholesterol to the Plasma Membrane in Exchange for Phosphatidylinositol 4, 5-Bisphosphate (PI(4,5)P2). Molecular Cell 73, 458–473.e457 (2019). [PubMed: 30581148]
43. Wang B et al. , Intestinal Phospholipid Remodeling Is Required for Dietary-Lipid Uptake and Survival on a High-Fat Diet. Cell Metabolism 23, 492–504 (2016). [PubMed: 26833026]
44. Lee SD, Thornton SJ, Sachs-Barrable K, Kim JH, Wasan KM, Evaluation of the Contribution of the ATP Binding Cassette Transporter, P-glycoprotein, to in Vivo Cholesterol Homeostasis. Molecular Pharmaceutics 10, 3203–3212 (2013). [PubMed: 23750858]
45. Folch J, Lees M, Sloane Stanley GH, A simple method for the isolation and purification of total lipides from animal tissues. Journal of Biological Chemistry 226, 497–509 (1957). [PubMed: 13428781]
46. Bligh EG, Dyer WJ, A rapid method of total lipid extraction and purification. Canadian Journal of Biochemistry and Physiology 37, 911–917 (1959). [PubMed: 13671378]
47. Bolger AM, Lohse M, Usadel B, Trimmomatic: a flexible trimmer for Illumina sequence data. Bioinformatics 30, 2114–2120 (2014). [PubMed: 24695404]

48. Dobin A et al. , STAR: ultrafast universal RNA-seq aligner. Bioinformatics 29, 15–21 (2013). [PubMed: 23104886]
49. Anders S, Pyl PT, Huber W, HTSeq—a Python framework to work with high-throughput sequencing data. Bioinformatics 31, 166–169 (2015). [PubMed: 25260700]
50. Love MI, Huber W, Anders S, Moderated estimation of fold change and dispersion for RNA-seq data with DESeq2. Genome Biology 15, 550 (2014). [PubMed: 25516281]
51. Hsieh W-Y et al. , Toll-Like Receptors Induce Signal-Specific Reprogramming of the Macrophage Lipidome. Cell Metabolism 32, 128–143.e125 (2020). [PubMed: 32516576]
52. Su B et al. , A DMS Shotgun Lipidomics Workflow Application to Facilitate High-Throughput, Comprehensive Lipidomics. Journal of the American Society for Mass Spectrometry 32, 2655–2663 (2021). [PubMed: 34637296]
53. Liebisch G et al. , High throughput quantification of cholesterol and cholesteryl ester by electrospray ionization tandem mass spectrometry (ESI-MS/MS). Biochim Biophys Acta 1761, 121–128 (2006). [PubMed: 16458590]
54. Preibisch S, Saalfeld S, Tomancak P, Globally optimal stitching of tiled 3D microscopic image acquisitions. Bioinformatics 25, 1463–1465 (2009). [PubMed: 19346324]
55. Sato T et al. , Single Lgr5 stem cells build crypt-villus structures in vitro without a mesenchymal niche. Nature 459, 262–265 (2009). [PubMed: 19329995]
56. Miyoshi H, Stappenbeck TS, In vitro expansion and genetic modification of gastrointestinal stem cells in spheroid culture. Nature Protocols 8, 2471–2482 (2013). [PubMed: 24232249]
57. Endapally S, Infante RE, Radhakrishnan A, in Intracellular Lipid Transport: Methods and Protocols, Drin G, Ed. (Springer New York, New York, NY, 2019), pp. 153–163.
58. Winter G, xia2: an expert system for macromolecular crystallography data reduction. Journal of Applied Crystallography 43, 186–190 (2010).
59. Evans PR, Murshudov GN, How good are my data and what is the resolution? Acta Crystallographica Section D 69, 1204–1214 (2013).
60. Winn MD et al. , Overview of the CCP4 suite and current developments. Acta Crystallographica Section D 67, 235–242 (2011).
61. McCoy AJ et al. , Ab initio solution of macromolecular crystal structures without direct methods. Proceedings of the National Academy of Sciences 114, 3637–3641 (2017).
62. Emsley P, Lohkamp B, Scott WG, Cowtan K, Features and development of Coot. Acta Crystallographica Section D 66, 486–501 (2010).
63. Langer GG, Hazledine S, Wiegels T, Carolan C, Lamzin VS, Visual automated macromolecular model building. Acta Crystallographica Section D 69, 635–641 (2013).
64. Murshudov GN et al. , REFMAC5 for the refinement of macromolecular crystal structures. Acta Crystallographica Section D 67, 355–367 (2011).
65. Liebschner D et al. , Macromolecular structure determination using X-rays, neutrons and electrons: recent developments in Phenix. Acta Crystallographica Section D 75, 861–877 (2019).

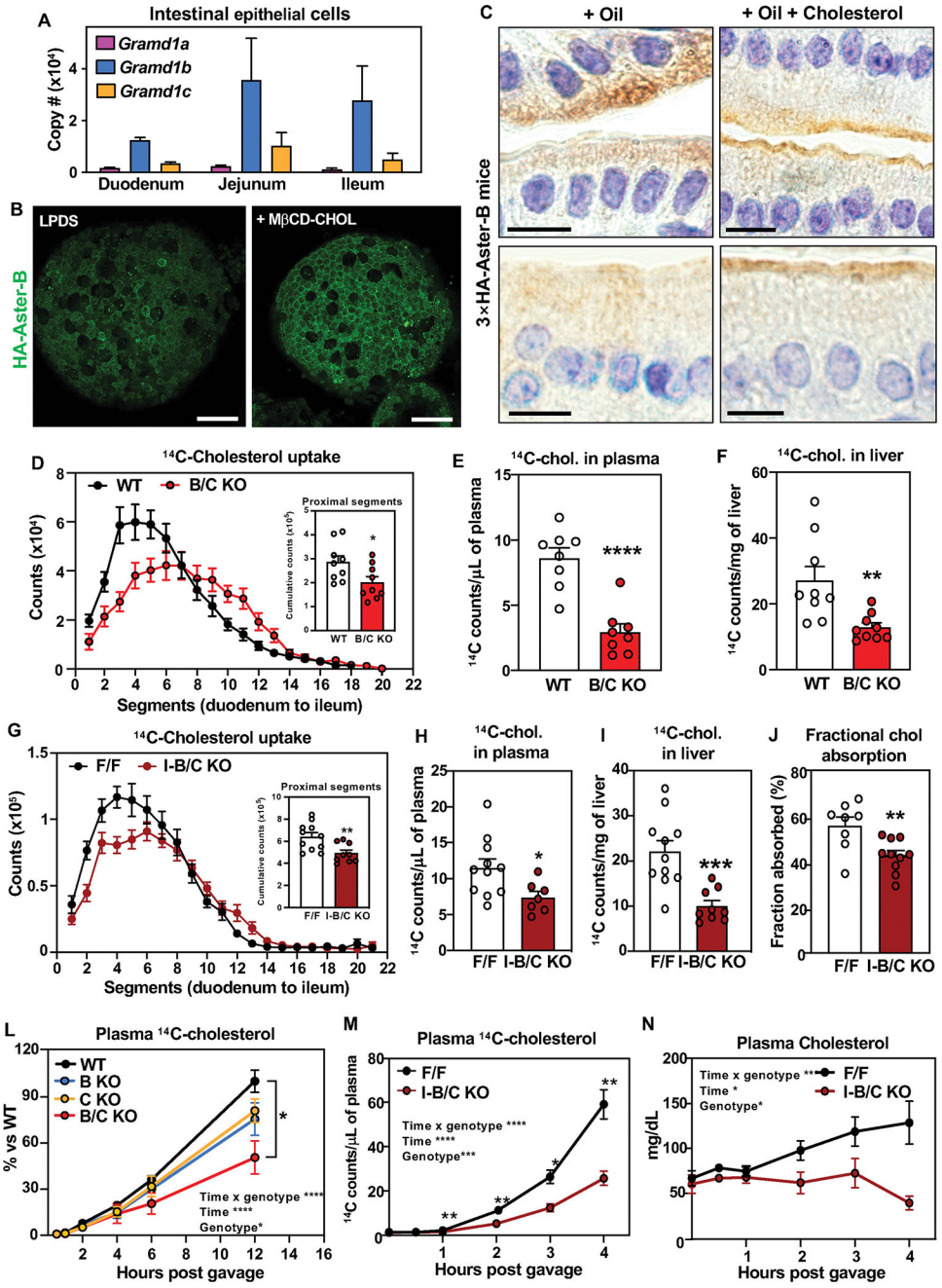

Fig. 1: Aster proteins modulate dietary cholesterol uptake.

(**A**) Absolute quantification of *Gramd1a/b/c* mRNA in duodenum, jejunum and ileum of C57BL/6J male mice (*n = 5*). (**B**) IF microscopy of HA-Aster-B in intestinal organoids from 3×HA-Aster-B mice during sterol deprivation (left) or loading with MβCD-cholesterol (right). Scale bar is 50 µm. (**C**) Immunohistochemical staining of HA-Aster-B in small intestines from 3×HA-Aster-B mice after a gastric gavage with corn oil or corn oil with cholesterol. For upper panels scale bar is 20 µm. panels. For lower panels scale bar is 10 µm. (**D**) Radioactivity in intestinal segments of female WT and B/C KO mice after oral gavage with olive oil containing [^{14}C]cholesterol for 2 h (*n = 9*/group), and cumulative counts in

the proximal intestine. (**E**) Radioactivity in plasma of mice described in D. (**F**) Radioactivity in livers of mice described in D. (**G**) Radioactivity in intestinal segments of female F/F and I-B/C KO mice after an oral challenge of olive oil containing [^{14}C]cholesterol for 2 h (*n = 9*/group), and cumulative counts in the proximal intestine. (**H**) Radioactivity in plasma of mice described in H. (**I**) Radioactivity in livers of mice described in I. (**J**) Cholesterol absorption measured by fecal dual-isotope ratio method (*n = 8–10*/group). (**K**) Kinetics of radioactivity in plasma of female WT (*n = 9*), BKO (*n = 5*), CKO (*n = 5*), B/C KO (*n = 5*) mice after an oral challenge of olive oil containing [^{14}C]cholesterol. (**L**) Kinetics of radioactivity in plasma of female F/F and I-B/C KO mice after injection of Poloxamer-407 and an oral challenge of [^{14}C]cholesterol in olive oil. (**N**) Kinetics of total cholesterol in mice described in L. Data are expressed as mean ± SEM. Statistical analysis: for panels D, E, F, G, H, I, J, unpaired *t* test; for panel L, 2-way ANOVA with Tukey's multiple comparisons test; for panels M and N, 2-way ANOVA with Sidak's multiple comparisons test. *p < 0.05, **p < 0.01, ***p < 0.001, ****p < 0.0001.

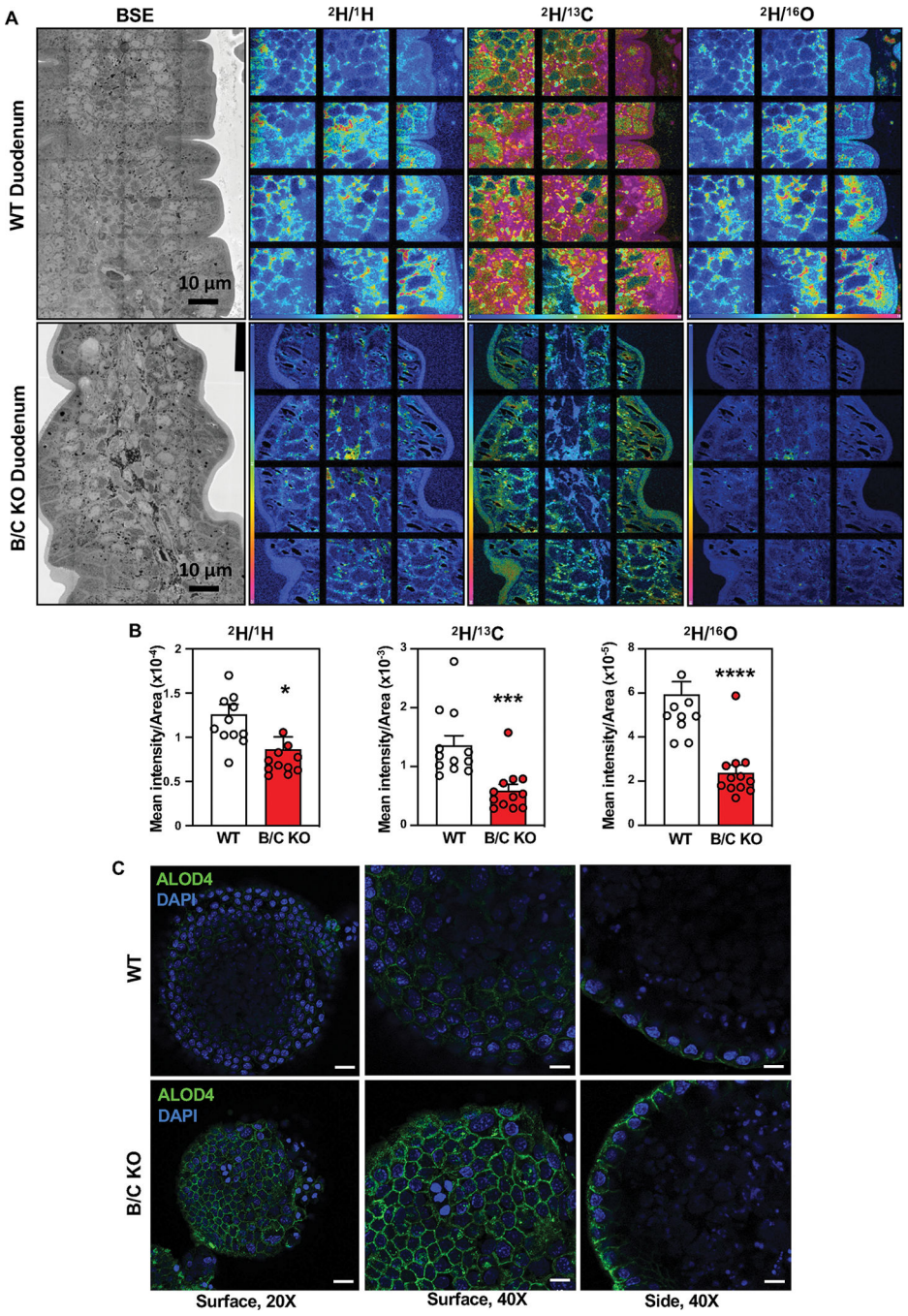

Fig. 2: Deletion of Asters reduces cholesterol internalization from the plasma membrane.

(**A**) Backscattered electron images and NanoSIMS images of a mid-duodenum villus from WT and B/C KO mice. (**B**) Quantification of the $^{2}H^{-}$ secondary ion signal, normalized to the $^{1}H^{-}$, $^{13}C^{-}$, and $^{16}O^{-}$ signals. (**C**) ALOD4 imaging of murine enteroids from WT and B/C KO mice 2 h after loading with MβCD cholesterol For left panels, scale bar is 20 µm. For middle and right panels scale bar is 10 µm. Data are expressed as mean ± SEM. Statistical analysis: unpaired *t* test; *p < 0.05, ***p < 0.001, ****p < 0.0001.

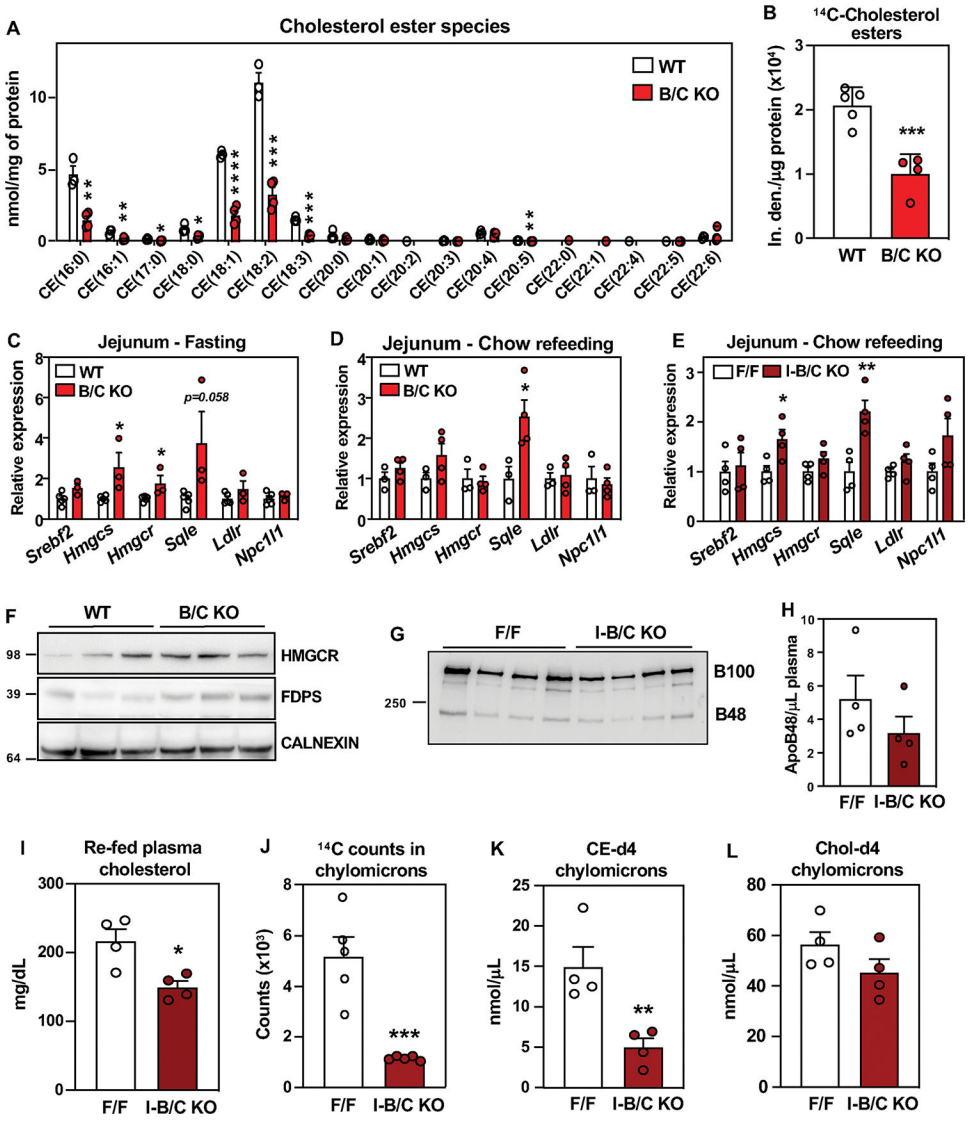

Fig. 3: Loss of Asters in intestine impairs cholesterol transfer to ER.

(**A**) Cholesterol ester quantification by mass spectrometry in proximal jejunum from WT (n = 3) and B/C KO *(n = 4)* 2 h post- refeeding a chow diet, after 10 h fasting. (**B**) Quantification of ^{14}C-labeled CE isolated from proximal jejunum scrapings of WT (*n = 5*) and B/C KO (*n = 4*) mice 2 h after oral gavage of [^{14}C]cholesterol. (**C**) Gene expression from distal jejunum scrapings of WT (*n = 5*) and B/C KO (*n = 3*) mice after 4 h of fasting. (**D**) Gene expression from distal jejunum scrapings of WT (*n = 3*) and B/C KO (*n = 4*) mice 2 h post- refeeding a chow diet, after 10 h fasting. (**E**) Gene expression from distal jejunum scrapings of F/F (*n = 4*) and I-B/C KO (*n = 4*) mice 2 h post-refeeding with chow diet, after 10 h fasting. (**F**) Western blot analysis of duodenum scrapings of mice described in D. (**G**) Western blot analysis and quantification of plasma from F/F (*n* = 4) and I-B/C KO (*n* = 4) mice fed for 21 days a high cholesterol (1.25%) diet, after 10 h of fasting followed by 2 h refeeding a HC diet. (H) ApoB48 quantified by densitometry and normalized on the volume of plasma used for WB detection. (**I**) Plasma cholesterol of mice described in

G. (**J**) Quantification of ^{14}C-counts in chylomicrons isolated from plasma of F/F (n=5) and I-B/C KO (n=5) 3 h after treatment with Poloxamer-407 and oral gavage of [^{14}C]cholesterol. (**K**), (**L**) Quantification of deuterated (-d4) CE (K) and free cholesterol (L) in chylomicrons isolated from plasma of F/F (n = 4) and I-B/C KO (n = 4) 3.5 h after treatment with Poloxamer-407 and oral gavage with cholesterol-d4. Data are expressed as mean ± SEM. Statistical analysis: unpaired t test, *p < 0.05, **p < 0.01, ***p < 0.001, ****p < 0.0001.

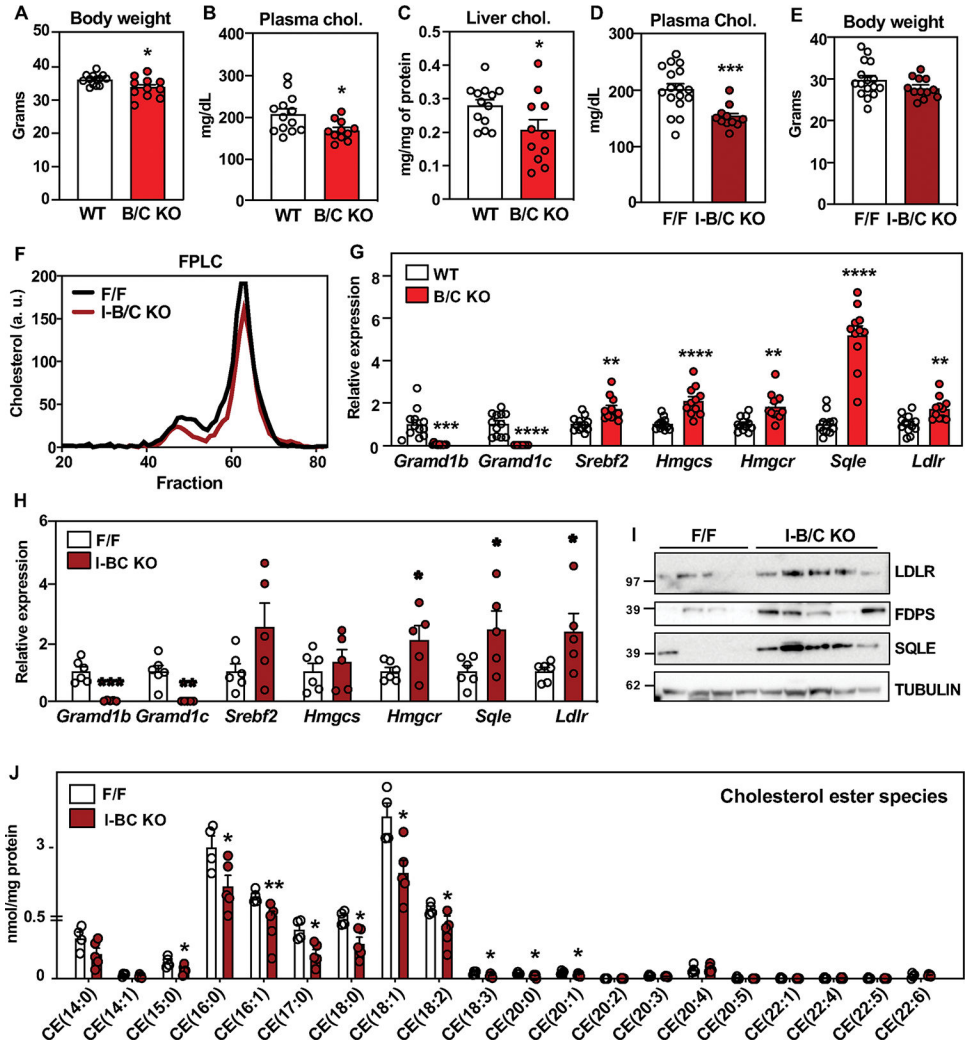

Fig. 4: Deletion of intestinal Asters protects from diet-induced hypercholesterolemia.

(**A**) Body weight of WT (*n = 13*) and B/C KO (*n = 11*) male mice after 21 days of a western diet + 1.25% cholesterol (HC). (**B**) Plasma cholesterol levels after 4 h fasting in mice described in A. (**C**) Liver cholesterol in mice described in A. (**D**) Plasma cholesterol levels after 4 h fasting in F/F (*n = 17*) and I-B/C KO (*n = 11*) male mice after 21 days of HC diet. (**E**) Body weight of mice described in D. (**F**) FPLC of plasma from F/F and I-B/C KO mice fed for 21 days with HC diet and euthanized after overnight fasting followed by 2 h of refeeding with the HC diet (pool of 3–5/group). (**G**) Gene expression in distal jejunum scrapings from WT (*n = 12*) and B/C KO (*n = 11*) mice after 21 days of HC diet, euthanized after 4 h fasting. (**H**) Gene expression in distal jejunum scrapings from F/F (*n = 6*) and I-B/C KO (*n = 5*) male mice after 21 days of HC diet, euthanized after 4 h fasting. (**I**) Western blot analysis of duodenum scrapings of mice described in H (*n = 4/5*). (**J**) Lipidomic analysis of CE in proximal jejunum scrapings from mice described in H (*n = 5*/group). Data are expressed as mean ± SEM. Statistical analysis: unpaired *t* test, *p < 0.05, **p < 0.01, ***p < 0.001, ****p < 0.0001.

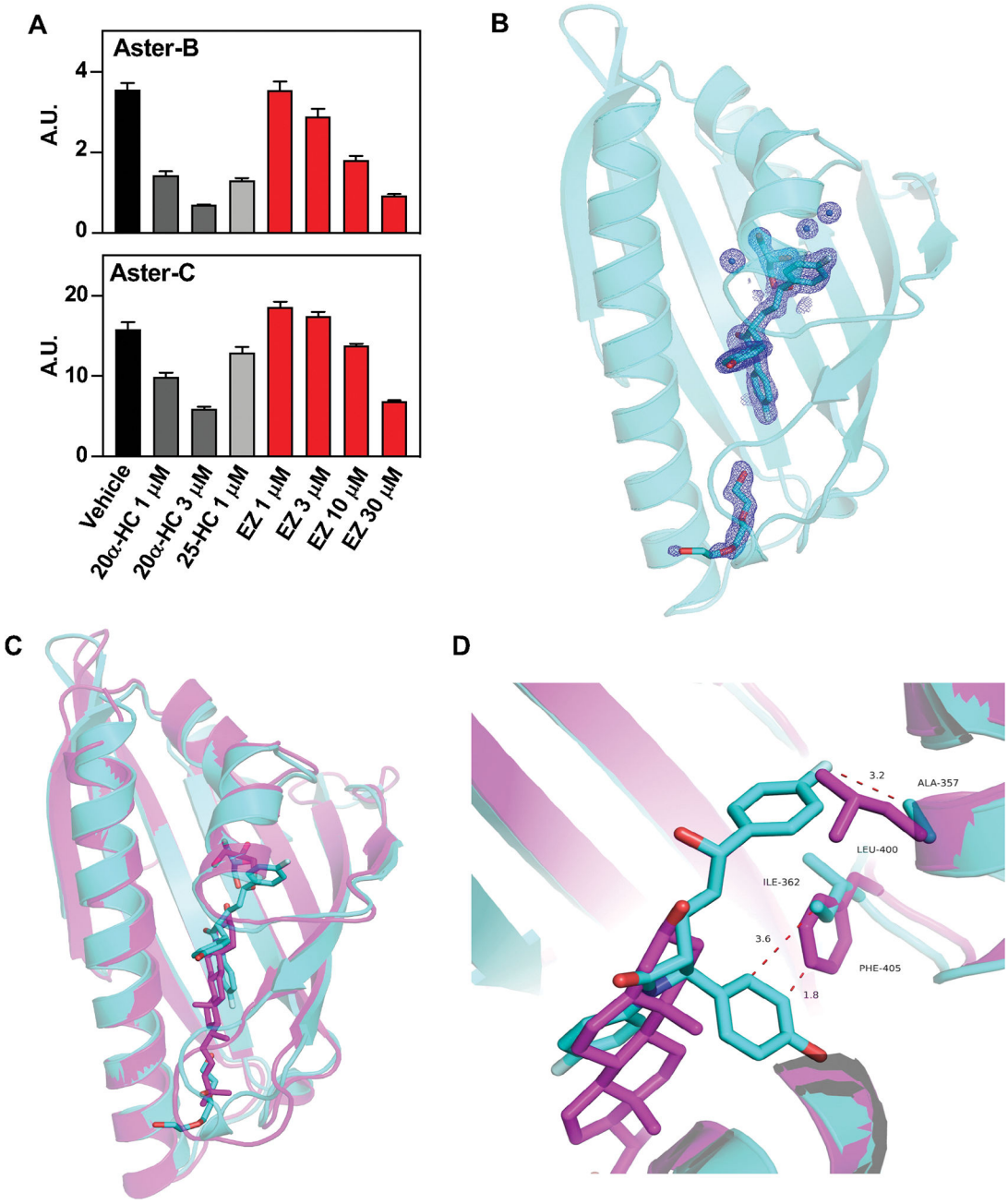

Fig. 5: Aster-B and Aster-C bind ezetimibe.

(**A**) Competition assays for 22-NBD-cholesterol binding to purified ASTER-B and ASTER-C domains incubated in presence of vehicle, 20α-HC, 25-HC, or EZ (1–30 mM). Data bars represent means ± SD. (**B**) Cartoon representation of the atomic structure, at 1.6 Å resolution, of the ASTER domain of Aster-C complexed to EZ. The EZ ligand in cyan sticks fits in a pocket created between the highly curved β-sheet, the second short helix, and the carboxyl-terminal helix. The cavity also accommodates glycerol (cyan sticks), water molecules (blue spheres), and part of a PEG 4000 molecule (cyan sticks). 2Fo-Fc electron density map of EZ, glycerol, part of PEG 4000, and water molecules in the binding cavity

shown as blue mesh contoured at 1.2σ. (**C**) Superposition of Aster-C:EZ (cyan) with the structure of Aster A:25-HC (pdb ID 6GQF). The overall architecture of the domain is very similar, but there are differences in the binding pocket and the opening loop. (**D**) Detail of the interaction between EZ and Aster-C involving residues ALA 357 and ILE 362, and superposition of the Aster-A:25-HC interaction. The superposition reveals how LEU 400 and PHE 405 from Aster A domain would clash with EZ, potentially preventing Aster A from binding EZ.

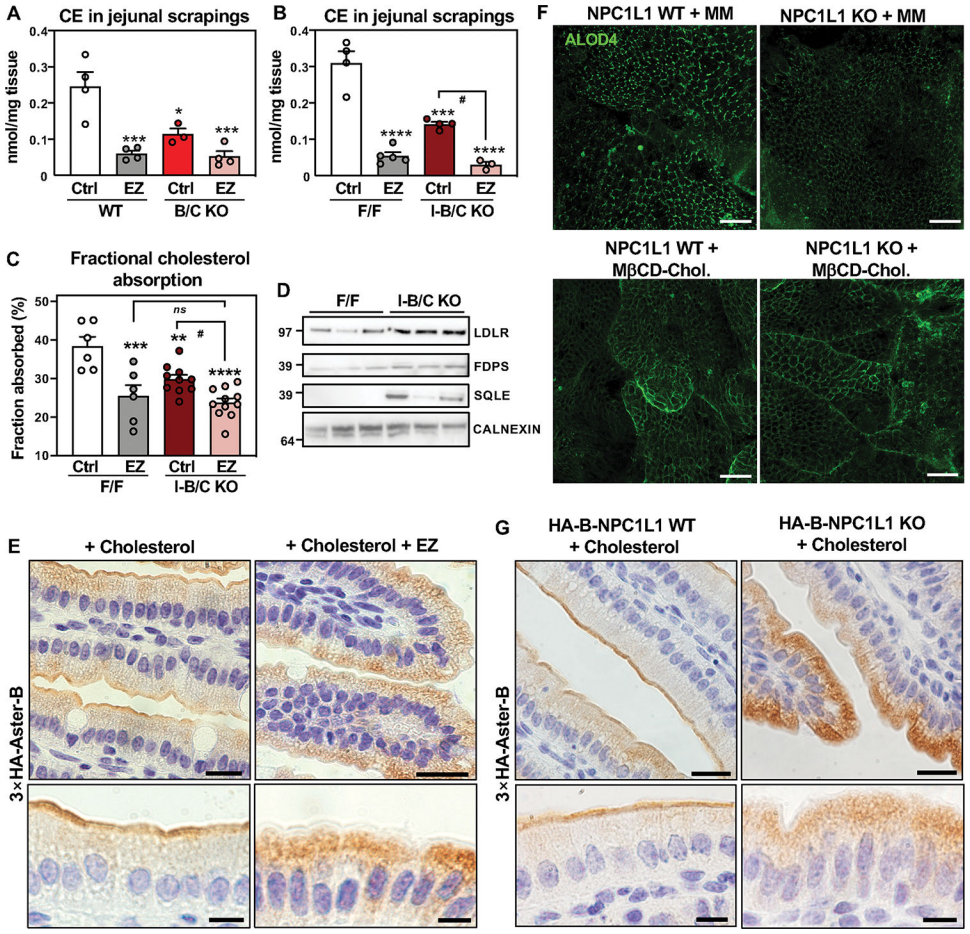

Fig. 6: NPC1L1 enriches accessible cholesterol at the brush border and promotes Aster recruitment.

(**A**) CE quantification by mass spectrometry in scrapings from proximal jejunum of WT and B/C KO mice fed for 3 days with a control diet (ctrl) containing 0.08% cholesterol or a diet containing 0.08% cholesterol and 0.01% EZ and euthanized after 10 h fasting followed by 2 h refeeding with the same diets (*n = 3–5*/group). (**B**) CE quantification by mass spectrometry in scrapings from proximal jejunum of F/F and I-B/C KO mice fed for 3 days with a control diet (ctrl) containing 0.08% cholesterol or a diet containing 0.08% cholesterol and 0.01% EZ) and euthanized 2 h after refeeding (*n = 3–5*/group). (**C**) Fractional absorption of cholesterol measured by fecal dual isotope method in F/F and I-B/C KO mice fed for 3 days with a control diet (ctrl) containing 0.08% cholesterol or a diet containing 0.08% cholesterol and 0.01% EZ. (**D**) Western blot analysis of duodenum scrapings from F/F and I-B/C KO mice fed for 3 days with EZ diet (*n = 3*/group). Samples were run on the same gel used for western blot analysis reported in Fig. S3F, therefore, the loading control (Calnexin) is the same. (**E**) Immunohistochemistry of HA-Aster-B in small intestines from 3×HA-Aster-B mice after an oral administration of vehicle or EZ and a gastric gavage with cholesterol in corn oil. (**F**) ALOD4 imaging of murine enteroids from WT and NPC1L1 KO mice after loading with cholesterol in mixed micelles or with MβCD-cholesterol. Scale bar is 40 μm. (**G**) Immunohistochemistry of HA-Aster-B in small intestines from 3×HA-Aster-B mice crossed to NPC1L1 WT or NPC1L1 KO mice after a gastric gavage with cholesterol in corn

oil. For E and G upper panels scale bar is 20 μm, for lower panels scale bar is 10 μm. Data are expressed as mean ± SEM. 2-way ANOVA with Tukey's multiple comparisons test. Data are expressed as mean ± SEM. *$p < 0.05$, **$p < 0.01$, ***$p < 0.001$, ****$p < 0.0001$ vs WT Ctrl, $^{\#}p < 0.05$ vs I-B/C KO Ctrl.

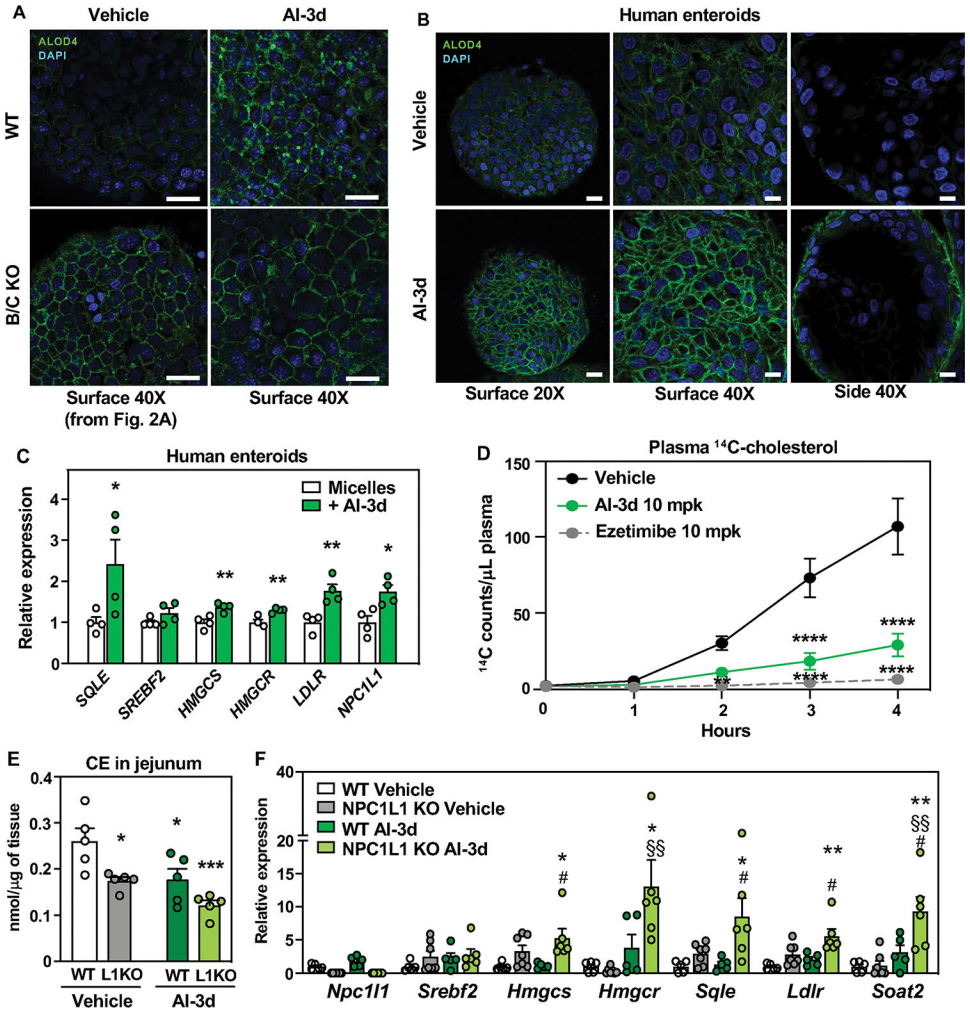

Fig. 7: Pharmacological inhibition of Asters reduces intestinal cholesterol uptake.

(**A**) ALOD4 staining (green) of PM accessible cholesterol in enteroids from WT and B/C KO mice loaded with MβCD cholesterol and treated with vehicle or Aster inhibitor AI-3d. Results presented in this panel and in Fig. 2C came from one experiment, where WT vehicle-treated enteroids served as control for both B/C KO vehicle-treated enteroids and for AI-3d vehicle-treated enteroids. Scale bar is 20 µm. (**B**) ALOD4 staining (green) of PM accessible cholesterol in human enteroids treated with vehicle or AI-3d. For left panels, scale bar is 20 µm. For middle and right panels, scale bar is 10 µm. (**C**) Gene expression of SREBP-2 and target genes in human enteroids differentiated on transwell plates and loaded with cholesterol in mixed micelles in the presence of vehicle or AI-3d. (**D**) Kinetics of radioactivity in plasma of female mice that were administered vehicle (*n = 6*), AI-3d (*n = 5*), or EZ (*n = 6*) in corn oil. After 1 h, the mice were given a gastric gavage of olive oil containing [^{14}C]cholesterol. (**E**) CE quantification by mass spectrometry in scrapings from proximal jejunum of NPC1L1 WT and NPC1L1 KO mice fed for 3 days with a control diet (ctrl) containing 0.08% cholesterol and treated with 3 doses of vehicle (left) or 10 mg/kg AI-3d (right) and euthanized after 10 h of fasting followed by 2 h refeeding with the same diet (*n = 5*/group). (**F**) Gene expression analysis of distal jejunum scrapings from mice

described in E. Statistical analysis for panel C, unpaired *t* test; for panels, D, E, F, 2-way ANOVA with Tukey's multiple comparisons test. Data are expressed as mean ± SEM. For panel C, *p < 0.05, **p < 0.01 vs micelles. For panel D **p < 0.01, ****p < 0.0001 vs Vehicle. For panels D, E *p < 0.05, **p < 0.01 vs WT Vehicle, $^{\#}$p < 0.05 vs WT AI-3d, §§ p < 0.01 vs NPC1L1 KO Vehicle.